PCCP

PAPER

View Article Online
View Journal | View Issue

Cite this: *Phys. Chem. Chem. Phys.*, 2025, **27**, 25862

An icosahedral Au_{13} nanocluster with three adjacent chlorides on opposite poles catalyses hydroamination of phenylacetylene

Shen Wu, Shinjiro Takano * and Tatsuya Tsukuda *

Received 6th September 2025,
Accepted 10th November 2025

DOI: 10.1039/d5cp03444b

rsc.li/pccp

A novel anionic gold nanocluster, $[Au_{13}(dppeF)_3Cl_6]^-$, bearing six chlorides, has been synthesized using a bulky diphosphine, dppeF (1,2-bis[bis(3,5-ditrifluoromethylphenyl)phosphino]ethane) as a protecting ligand. Single-crystal X-ray diffraction analysis revealed that this nanocluster has an icosahedral Au_{13} core, which is protected by each of three Cl ligands on opposite poles and by three dppeF ligands in an equatorial plane. This nanocluster acted as a homogeneous catalyst for hydroamination between phenylacetylene and aniline, facilitated by the rapid exchange of the Cl^- ligands with phenyl acetylides.

Introduction

In recent decades, the development of ligand-protected gold nanoclusters (AuNCs) has emerged as a significant area of research, due to their unique properties, which can be finely adjusted through the precise control of their size, shape, and surface modifications.[1–3] Phosphines are some of the most common types of ligands used to protect AuNCs.[4–9] Among numerous phosphine-protected AuNCs reported, icosahedral Au_{13} NCs protected by alkyl-bridged diphosphines (L = Ph_2-P-$(CH_2)_n$-PPh_2; n = 1–5) provide an ideal opportunity to demonstrate how the ligand structure can precisely adjust the geometric structure, stability, and physicochemical properties of AuNCs. The chemical formulas in Table 1 show that the L/Cl ratio in the Au_{13} NC depends on the n value of L.[10–12] The observed trend suggests that one bulkier L is replaced by two less bulky Cl ligands. This exchange decreases the total charge by two, keeping the total number of valence electrons at eight. Based on the sequence of chemical formulas in Table 1, we can predict that a negatively charged NC, such as $[Au_{13}L_3Cl_6]^-$, will form when L is bulkier than dpppe.

The structure of L affects not only the L/Cl ratio but also the structure and optical properties of the Au_{13} core.[13–17] The Au_{13} core of $[Au_{13}(dppe)_5Cl_2]^{3+}$ (**Au_{13}:dppe**) is a nearly perfect icosahedron, whereas that of $[Au_{13}(dppm)_6]^{5+}$ (**Au_{13}:dppm**) is significantly distorted into D_3 symmetry, probably due to the mechanical stress imposed on the two P sites of dppm. **Au_{13}:dppe** exhibits photoluminescence (PL) at 766 nm with a quantum yield (QY) of 8%.[11] The PLQY drops to 0.8% for $[Au_{13}(dppe)_4Cl_4]^+$ (**Au_{13}:dppp**) and is below the detection limit for **Au_{13}:dppm**.

This work aimed at developing atomically precise AuNC catalysts with a Cl-rich surface. The idea comes from a report that the hydrochlorination of phenylacetylene (PA-H) was catalysed by a halide-rich AuNC: $[Au_{13}(NHC)_6Br_6]^-$ (NHC = N-heterocyclic carbene).[14] We attempted to synthesize a Cl-rich Au_{13} NC using $(Ar^F)_2PC_2H_4P(Ar^F)_2$ (Ar^F = 3,5-bis(trifluoromethyl)-phenyl; dppeF) as a ligand, which is bulkier than dppe due to the presence of multiple CF_3 groups within an otherwise identical molecular framework. We also expect that the resulting Au_{13} core will be stabilized electronically by the CF_3 groups *via* an inductive mechanism.[18] We successfully obtained $[Au_{13}(dppeF)_3Cl_6]^-$ (**Au_{13}:dppeF**) (Table 1) and determined its structure using single-crystal X-ray diffraction (SCXRD) analysis. **Au_{13}:dppeF** has an icosahedral Au_{13} core that is surrounded by three dppeF ligands at the equator and six Cl ligands at the axial Au_3 triangles on opposite poles. The superatomic nature of the Au_{13} core was confirmed by density functional theory (DFT) calculations. **Au_{13}:dppeF** exhibited higher catalytic activity than **Au_{13}:dppe** for the hydroamination of PA-H using aniline as the nucleophile.[19] The reaction pathways were probed

Table 1 Au_{13} NCs protected by alkyl-bridged diphosphines

Formula	L	Ref.
$[Au_{13}L_6]^{5+}$	Ph_2P-$(CH_2)_1$-PPh_2 (dppm)	10
$[Au_{13}L_5Cl_2]^{3+}$	Ph_2P-$(CH_2)_2$-PPh_2 (dppe)	11
$[Au_{13}L_4Cl_4]^+$	Ph_2P-$(CH_2)_3$-PPh_2 (dppp)	12
	Ph_2P-$(CH_2)_4$-PPh_2 (dppb)	
	Ph_2P-$(CH_2)_5$-PPh_2 (dpppe)	
$[Au_{13}L_3Cl_6]^-$	$(Ar^F)_2P$-$(CH_2)_2$-$P(Ar^F)_2$ (dppeF)	This study

(Ar^F = 3,5-bis(trifluoromethyl)phenyl).

Department of Chemistry, Graduate School of Science, The University of Tokyo, 7-3-1 Hongo, Bunkyo-ku, Japan. E-mail: stakano@chem.s.u-tokyo.ac.jp, tsukuda@chem.s.u-tokyo.ac.jp

using *in situ* electrospray ionization mass spectrometry (ESI-MS) by taking advantage of homogeneous catalytic conditions.[20–27] Based on the reaction intermediates detected by *in situ* ESI-MS, we propose that the reaction starts with the activation of PA-H *via* ligand exchange with Cl, followed by attack by a nucleophile (aniline) to produce the corresponding enamine, which releases imine as a final product.

Results and discussion

Synthesis and structural characterization of Au_{13}:dppeF

A tetraphenylphosphonium (PPh_4^+) salt of **Au_{13}:dppeF** was synthesized using a method analogous to the one used to prepare **Au_{13}:dppe**.[11] The synthetic details are provided in the Supporting Information (SI). Briefly, the $(AuCl)_2$dppeF complex in tetrahydrofuran was reduced by $NaBH_4$ at 253 K. The resultant polydispersed mixture of dppeF-protected AuNCs was subjected to an HCl etching process to focus the AuNC sizes. **Au_{13}:dppeF** was recrystallized from dichloromethane and hexane after alumina column chromatography and repeated reprecipitation, yielding black crystals. The yield was 35% based on Au.

Fig. 1a presents a typical negative-mode ESI mass spectrum of (PPh_4^+)·**Au_{13}:dppeF**. The intense mass peak was assigned to the formula of $[Au_{13}(dppeF)_3Cl_6]^-$, as confirmed by comparing the experimental and the calculated isotope patterns. To the best of our knowledge, this is the first example of a negatively charged Au_{13} NC protected by phosphines. Fig. 1b shows the ultraviolet-visible (UV-Vis) absorption spectra of acetonitrile solutions of **Au_{13}:dppeF** and **Au_{13}:dppe**, which were prepared by dissolving crystals of (PPh_4^+)·**Au_{13}:dppeF** and **Au_{13}:dppe**·$(PF_6^-)_3$, respectively. Both spectra exhibit characteristic peaks that reflect the quantized electronic structures. The spectral profiles of **Au_{13}:dppeF** and **Au_{13}:dppe** are similar, but do not match due to their structural differences. The energy gap between the highest occupied molecular orbital (HOMO) and the lowest unoccupied molecular orbital (LUMO) of **Au_{13}:dppeF** is estimated to be 2.0 eV from a spectral onset of the UV-Vis absorption spectrum. This value is comparable to that of **Au_{13}:dppe** (~1.9 eV).[8,11,16] By combining with the nuclear magnetic resonance (NMR) data of (PPh_4^+)·**Au_{13}:dppeF** (Fig. S1), we concluded that the target Au_{13} NC with six chlorides was successfully obtained.

Next, we examined the geometric structure of **Au_{13}:dppeF** using SCXRD analysis. (PPh_4^+)·**Au_{13}:dppeF** crystallized in the triclinic crystal system with the $P\bar{1}$ space group (Table S1). Fig. 2a shows the determined structure of **Au_{13}:dppeF** and reveals that it has an icosahedral Au_{13} core. The continuous symmetry measure (CSM),[28] which quantifies deformation from an ideal icosahedron (CSM = 0), was calculated to be 0.029 for the Au_{13} core in **Au_{13}:dppeF**. This value is closer to 0 than that of **Au_{13}:dppe** (CSM = 0.036)[8] and indicates that the Au_{13} core of **Au_{13}:dppeF** is a nearly perfect icosahedron. Fig. 2b shows the coordination geometry of the ligands around the Au_{13} core. Three dppeF ligands coordinate with the Au_6 ring in a chair configuration on the equator of the Au_{13} core. The remaining axial Au_3 triangles at the top and bottom are fully capped by three chlorides each, giving pseudo-C_3 symmetry along the axial direction. Halide-accumulated facets were also observed in $[Au_{13}(NHC)_6Br_6]^-$, but they were divided into asymmetric sites of Br_4 and Br_2.[14] These results imply that halides tend to segregate on the AuNC surface. However, the limited examples of polyhalogenated Au_{13} NCs make it difficult to conclude whether the segregated behavior of halides is a general feature.

The electronic structure of **Au_{13}:dppeF** was investigated using DFT calculations with a full ligand model. Structural optimization was conducted using the crystal structure of **Au_{13}:dppeF** as the initial structure. The optimized structure, shown in Fig. S2, reproduced the crystal structure shown in Fig. 2. Fig. 3 shows the energy diagrams and the corresponding Kohn–Sham (KS) orbitals of **Au_{13}:dppeF**. As expected, given the eight valence electrons calculated for **Au_{13}:dppeF**, the HOMO, HOMO−1, and HOMO−2 are assigned to three 1P superatomic orbitals. This confirms the electron configuration of $(1S)^2(1P)^6$. Despite the nearly perfect icosahedral Au_{13} core, the 1P orbitals are split into two subgroups, $1P_z$ and $1P_x/1P_y$. The $1P_z$ orbital is more stable than the $1P_x/1P_y$ orbitals due to electrostatic stabilization by the six electron-withdrawing chlorides located along the *z*-axis. This also explains why the $1D_{z^2}$ orbital distributed along the *z* axis corresponds to the LUMO. The

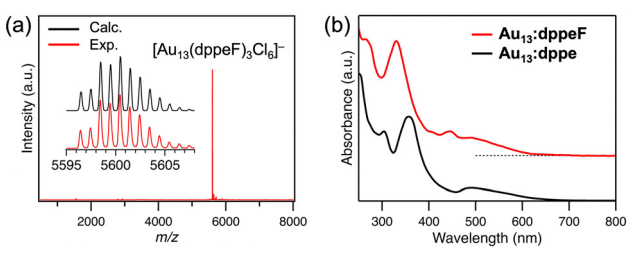

Fig. 1 (a) Negative-mode ESI mass spectrum of (PPh_4^+)·**Au_{13}:dppeF**. The inset compares the isotope patterns experimentally observed (red) and calculated (black) for **Au_{13}:dppeF**. (b) UV-Vis absorption spectra of (PPh_4^+)·**Au_{13}:dppeF** (red) and **Au_{13}:dppe**·$(PF_6^-)_3$ (black) in acetonitrile.

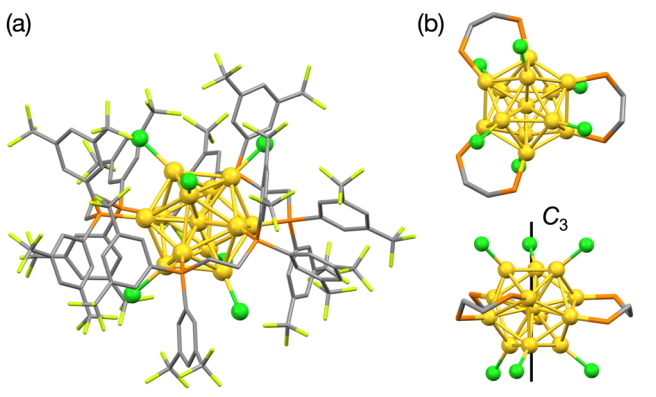

Fig. 2 (a) The entire structure of **Au_{13}:dppeF**, as determined by SCXRD analysis. (b) Top and side views of **Au_{13}:dppeF**. Hydrogen atoms, Ar^F moieties, a solvent molecule, and the PPh_4^+ ion are omitted for clarity. Color code: Au, yellow; P, orange; Cl, green; C, gray; F, yellow-green.

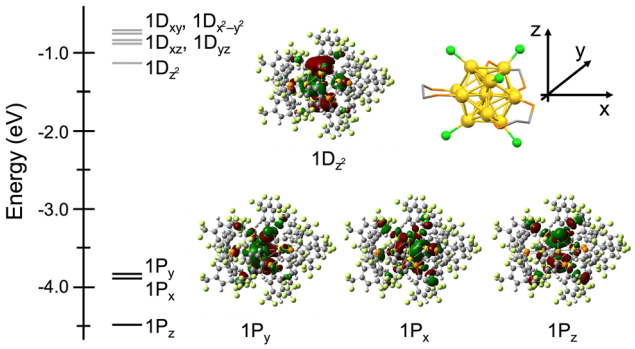

Fig. 3 Energy diagrams and KS orbitals of **Au$_{13}$:dppeF** (isovalue = 0.02). The top-right figure shows the orientation of the **Au$_{13}$:dppeF** NC without the Ar^F moieties and H atoms, which have been removed for clarity.

HOMO–LUMO gap was calculated to be 2.6 eV, which is larger than 2.0 eV determined by the optical method. A similar overestimation was observed in the case of **Au$_{13}$:dppe**.[13]

Catalytic application of Au$_{13}$:dppeF to hydroamination reaction

Fig. 4 compares the space-filling models of **Au$_{13}$:dppeF** and **Au$_{13}$:dppe**. The Au$_{13}$ core surface of **Au$_{13}$:dppeF** is clearly visible through the gap between the three Cl ligands. In contrast, the Au$_{13}$ core of **Au$_{13}$:dppe** is barely visible. This remarkable difference in the steric environment suggests that reactants can readily access the Au$_{13}$ core of **Au$_{13}$:dppeF** than that of **Au$_{13}$:dppe**. The catalytic application of well-defined AuNCs can provide useful information for establishing a correlation between structure and catalysis.[29–32] Inspired by the hydrochlorination of PA-H by the halide-rich $[Au_{13}(NHC)_6Br_6]^-$,[14] we compared the catalytic activity of **Au$_{13}$:dppeF** and **Au$_{13}$:dppe** for the hydroamination of terminal alkynes by amines under homogeneous conditions. PA-H and aniline were selected as the model terminal alkyne and amine, respectively.[19] As shown in Table 2, **Au$_{13}$:dppeF** catalysed the reaction (entry 1): the conversion after 24 h was 29% (Fig. S3), increasing up to ~95% after two weeks. Conversion after 24 h increased with the amount of **Au$_{13}$:dppeF** loading and reached up to 82% at 0.040 mol% (entries 2–4). The gradual decrease in TON values with increasing catalyst loading (entries 2–4) is due to the decreasing substrate concentration. In contrast, the conversions after 2 h were nearly proportional to the catalyst concentration, and TON values remained constant (Table S2). These results suggest that the active sites of the catalyst are uniform, despite the presence of multiple halide sites. The blank test (entry 10) and the poor conversion by the $(AuCl)_2$-dppeF complex (entry 8) indicate that the higher conversion is associated with **Au$_{13}$:dppeF**. Conversion by **Au$_{13}$:dppeF** was higher than that by **Au$_{13}$:dppe** (entry 9). This result supports our hypothesis that the less crowded chlorinated area provides the active site.

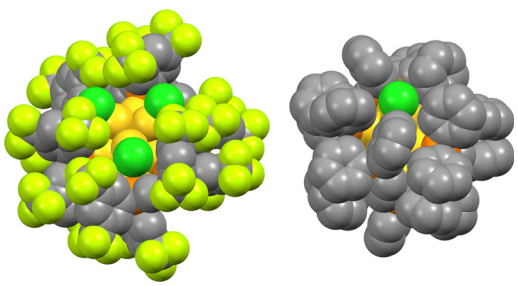

Fig. 4 Space-filling models of **Au$_{13}$:dppeF** (left) and **Au$_{13}$:dppe** (right) around the Cl coordination sites. Color code: Au, yellow; P, orange; Cl, green; C, gray; F, yellow-green.

Table 2 Catalytic activity of Au$_{13}$ NCs in the hydroamination of PA-H with aniline[a]

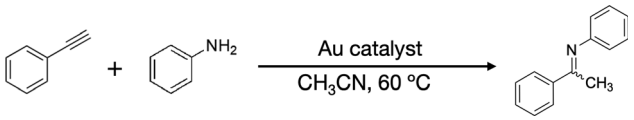

Entry	Catalyst	mol%[b]	Conversion (%)	TON[c]
1	**Au$_{13}$:dppeF**	0.010	29	2.9×10^3
2	**Au$_{13}$:dppeF**	0.015	41	2.7×10^3
3	**Au$_{13}$:dppeF**	0.027	67	2.4×10^3
4	**Au$_{13}$:dppeF**	0.040	82	2.1×10^3
5	**Au$_{13}$:dppeF/Br**	0.0098	6.3	6.3×10^2
6	**Au$_{13}$:dppeF/I**	0.010	<1	n.d.[d]
7	**Au$_{13}$:dppeF/PA**	0.011	32	3.2×10^3
8	$(AuCl)_2$-dppeF	0.065	9.1	1.4×10^2
9	**Au$_{13}$:dppe**	0.010	4.8	4.8×10^2
10	blank	—	<1	n.d.[d]

[a] General conditions: PA-H (1.0 M), aniline (5.0 M), 500 rpm, 24 h. Conversion was estimated by ^{1}H NMR analysis using 1,3,5-trimethoxybenzene as an internal standard. [b] Molecular base. [c] TON = Conversion (%)/mol%. [d] Not determined.

It has been reported that the Cl ligands in **Au$_{13}$:dppe** can be replaced by PA$^-$.[13] To confirm that the same ligand exchange occurs in **Au$_{13}$:dppeF**, we measured the ESI mass spectra of a mixed solution of **Au$_{13}$:dppeF** and 50 equivalents of PA-H in the presence of the Brønsted base triethylamine. As expected, the dominant species detected was the fully PA-exchanged AuNCs $[Au_{13}(dppeF)_3(PA)_6]^-$ (**Au$_{13}$:dppeF/PA**) (Fig. S4). This observation led us to hypothesize that **Au$_{13}$:dppeF** undergoes ligand exchange from Cl to PA, and that the resultant PA-functionalized Au$_{13}$ NCs are involved in the catalytic reactions. To investigate this possibility, we characterized the AuNCs after a 24-hour catalytic reaction of **Au$_{13}$:dppeF** using ESI-MS. As shown in Fig. S5, the main species detected was the fully PA-exchanged AuNCs **Au$_{13}$:dppeF/PA**. We also studied the catalytic activity of the pre-synthesized **Au$_{13}$:dppeF/PA**. As shown in entry 7 of Table 2, the catalytic activity of **Au$_{13}$:dppeF/PA** was slightly higher than that of **Au$_{13}$:dppeF** (entry 1, Table 2). These results suggest that the PA ligands introduced onto the Au$_{13}$ NCs are key to hydroamination by aniline.

To further support the above suggestions, we examined the impact of halogens on activity. To this end, we synthesized the halide-exchanged analogues $[Au_{13}(dppeF)_3Br_6]^-$ (**Au$_{13}$:dppeF/Br**) and $[Au_{13}(dppeF)_3I_6]^-$ (**Au$_{13}$:dppeF/I**) by mixing **Au$_{13}$:dppeF** with KBr and KI, respectively.[15] The synthetic details and characterization results are provided in the SI (Fig. S6–S9). SCXRD analysis of the halide-exchanged products revealed

the same coordination geometry (Fig. S10 and Table S1), indicating that these NCs can provide direct insight into the effect of halides on the catalytic activity. As shown in entries 1, 5, and 6 of Table 2, the reactivity decreases in the following order: **Au_{13}:dppeF** > **Au_{13}:dppeF/Br** ≫ **Au_{13}:dppeF/I**. This trend reveals that the nature of the halides significantly affects activity. To elucidate halide-dependent catalytic activity, we compared the ligand exchange activity of **Au_{13}:dppeF**, **Au_{13}:dppeF/Br**, and **Au_{13}:dppeF/I** with the PA^- ligands using ESI-MS. We added 10 equivalents of PA-H to solutions of **Au_{13}:dppeF**, **Au_{13}:dppeF/Br**, and **Au_{13}:dppeF/I**, in the presence of 10 equivalents of triethylamine, to promote the deprotonation of the terminal alkynyl proton. Fig. S11 shows the SI mass spectra of the mixed solutions after 24 h. Partially or fully PA-exchanged AuNCs $[Au_{13}(dppeF)_3(PA)_nX_{6-n}]^-$ (X: Cl, Br, or I) were detected similarly. The average number of PA ligands introduced (n) was ~1.6, ~0.3, and <0.1 for **Au_{13}:dppeF**, **Au_{13}:dppeF/Br**, and **Au_{13}:dppeF/I**, respectively. These numbers increased to 5.9, 4.1, and 0.3, respectively, after 24 h of the catalytic reaction, where an excess of PA-H is present (Fig. S12). These results indicate that reactivity toward PA exchange decreased in the following order: **Au_{13}:dppeF** > **Au_{13}:dppeF/Br** ≫ **Au_{13}:dppeF/I**. This is consistent with the activity order shown in entries 1, 5 and 6 of Table 2. Fig. S13 shows the time-course results for the catalysts of **Au_{13}:dppeF**, **Au_{13}:dppeF/Br**, **Au_{13}:dppeF/I** and **Au_{13}:dppeF/PA** (entries 1 and 5–7, Table 2). These results suggest that activating the PA ligands on Au_{13} *via* ligand exchange is a critical step in the reaction.

The catalytic hydroamination reaction has been studied using an Au complex,[33] an Au surface,[34] Au nanoparticles (AuNPs),[35–37] and AuNCs.[19] All of these Au catalysts, except for the AuNCs, activate PA-H *via* a π-bond on an Au atom while leaving the terminal hydrogen atoms intact, as shown in Fig. 5a. In the case of $[Au_{16}(bi\text{-}NHC)_5(PA)_3Br_2]^{3+}$ (bi-NHC = bidentate NHC ligand),[19] although PA forms novel surface units of (bi-NHC)–Au(I)–PA on the icosahedral Au_{13} core, it is π-bonded to the Au_{13} core. Contrary to these examples, we propose σ-bonding of PA to the Au_{13} core of **Au_{13}:dppeF** (Fig. 5b), based on the SCXRD result of a similar system, $[Au_{13}(dppe)_5(PA)_2]^{3+}$.[13] To further support this hypothesis, DFT structural optimization was conducted for **Au_{13}:dppeF/PA** by replacing six Cl ligands of **Au_{13}:dppeF** with σ-ligated PA ligands. The optimized structure, shown in Fig. S14, supports σ-bonding of PA to the Au_{13} NC. The difference in the PA bonding mode is likely due to the difference in the steric environment at the adsorption site: σ-bonding is preferred at sterically crowded sites, while π-bonding is possible only at sterically open sites. The σ-bonding of PA to the Au_{13} NC alters the charge distribution of the PA molecule *via* electronic coupling between the 1P superatomic orbital of the Au_{13} core and the π orbital of the PA molecule, as theoretically demonstrated by Konishi.[13] According to the natural bond orbital (NBO) analysis of our DFT-optimized structures of **Au_{13}:dppeF/PA** and free PA^-, the electronic charge transfers from PA to the Au_{13} NC. The NBO charges of the terminal C (C_α) and the adjacent C (C_β) atoms of the PA ligand suggest that C_α becomes electron-rich and C_β becomes electron-deficient upon ligation (Table S3).

Based on the above discussions, we propose the following catalytic mechanism for **Au_{13}:dppeF**, as depicted schematically in Fig. 5c. The reaction begins with ligand exchange with PA-H in the presence of excess aniline, which acts as a Brønsted base (step i). Next, the σ-bonded PA is attacked by the nucleophile aniline. The nucleophilic attack by aniline occurs at the electron-deficient C_β, to produce an enamine according to the Markovnikov rule (step ii). This nucleophilic attack of aniline on the σ-bonded PA substrate has also been proposed as a key step in the catalysis of Au_{16} NC.[19] Finally, enamine tautomerizes to the imine (step iii), and then protodeauration and ligand exchange with a new PA occur (step iv).

Finally, we evaluated the stability of **Au_{13}:dppeF** during the catalytic reaction. After 24 h of the reaction, we collected the catalysts by evaporating the solvent, followed by washing with a toluene–hexane mixture (1 : 3) to remove the remaining reactants and the products. The precipitate exhibited a similar UV-Vis absorption profile to that of (PPh_4^+)·**Au_{13}:dppeF/PA** (Fig. 6), which is consistent with the ESI-MS results. The catalysts after the 1st and 2nd usage exhibited similar spectral profiles (Fig. 6). These results suggested that the NC retained its

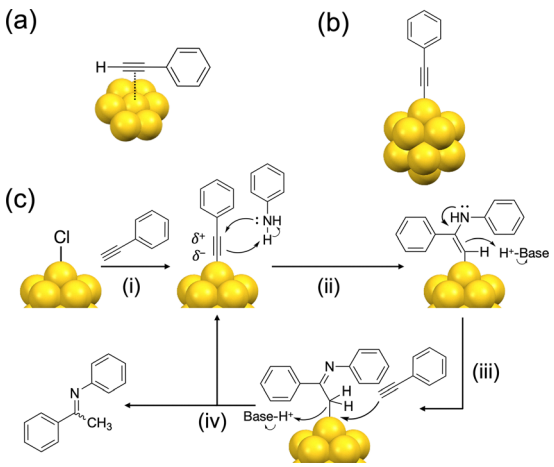

Fig. 5 Schematic representation of (a) π-ligation of PA-H to an Au surface and (b) σ-bonding of PA to Au NC. (c) Proposed reaction mechanism of hydroamination of PA-H on Au_{13} NCs.

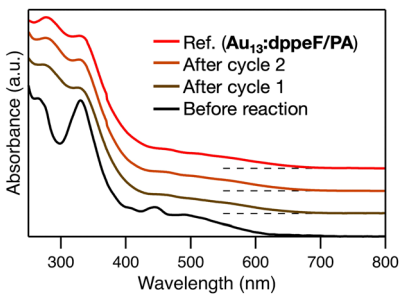

Fig. 6 UV-Vis absorption spectra of initial **Au_{13}:dppeF** (black) and **Au_{13}:dppeF** after cycles 1 (dark brown) and 2 (brown), along with the spectrum of **Au_{13}:dppeF/PA** (red) as a reference.

Table 3 Recycling test of catalytic activity of **Au_{13}:dppeF**[a]

Cycle	Weight (mg)[b]	mol%[c]	Conversion (%)	TON[d]
1	6.0	0.010	29	2.9×10^3
2	3.9	0.0061[e]	19	3.1×10^3
3	2.3	0.0036[e]	11	3.0×10^3

[a] General conditions: PA-H (1.0 M), aniline (5.0 M), 500 rpm, 24 h. Conversion was estimated by ^{1}H NMR analysis using 1,3,5-trimethoxybenzene as an internal standard. [b] Weight of the loading catalyst in each run. [c] Molecular base. [d] TON = Conversion (%)/mol%. [e] Calculated as **Au_{13}:dppeF/PA**.

Au_{13}:dppeF/PA structure, indicating the stability of Au NCs during the catalysis. We also compared catalytic activity during recycled usage. The conversion by 0.01 mol% catalyst decreased from 32% to 19% and 11%, respectively, in the 2nd and 3rd cycles (Table 3). The gradual reduction in conversion with reuse is due to the reduced recovery of **Au_{13}:dppeF/PA** NCs by washing with a toluene–hexane mixture. The weight of the recovered catalyst was reduced to ~60% of the original value by washing (Table 3). Assuming the recovered precipitate was pure **Au_{13}:dppeF/PA** NCs, the TON at the 2nd and 3rd cycles was calculated to be 3.1×10^3 and 3.0×10^3, respectively (Table 3). These values closely match the TON for **Au_{13}:dppeF/PA** (3.2×10^3, entry 7, Table 2), which reinforces the high durability of this NC.

Conclusions

We successfully synthesized an anionic Au_{13} NC with six Cl ligands by using bulky diphosphines as protecting ligands. Single-crystal X-ray diffraction analysis revealed that the six chlorides coordinate with the two Au_3 facets located at opposite poles of the icosahedral Au_{13} core. The Au_{13} NC was then used to catalyse the hydroamination reaction between PA-H and aniline to form an enamine. Based on the reaction intermediates detected by *in situ* ESI-MS, we propose that the reaction begins with the dissociative adsorption of PA-H, while releasing a Cl ligand. Then, a nucleophile aniline attacks at the electron-deficient C_β of the adsorbed PA, producing the corresponding enamine. The efficient introduction of PA was attributed to the less crowded environment of the Cl-accumulated Au_3 facets.

Author contributions

S. Wu: investigation, visualization, writing – original draft, writing – review & editing. S. Takano: conceptualization, investigation, funding acquisition, supervision, validation, writing – original draft, writing – review & editing. T. Tsukuda: conceptualization, funding acquisition, resources, supervision, writing – review & editing.

Conflicts of interest

There are no conflicts to declare.

Data availability

The data supporting this article have been included as part of the supplementary information (SI). Supplementary information is available. See DOI: https://doi.org/10.1039/d5cp03444b.

CCDC 2481066, 2484473 and 2484474 contain the supplementary crystallographic data for this paper.[38a–c]

Acknowledgements

This work was financially supported by JST CREST (grant number: JPMJCR20B2) and JSPS KAKENHI grants (no. JP23H00284 and JP23K26610).

Notes and references

1 R. Jin, C. Zeng, M. Zhou and Y. Chen, *Chem. Rev.*, 2016, **116**, 10346.
2 I. Chakraborty and T. Pradeep, *Chem. Rev.*, 2017, **117**, 8208.
3 X. Zou, X. Kang and M. Zhu, *Chem. Soc. Rev.*, 2023, **52**, 5892.
4 B. K. Teo and H. Zheng, *Coord. Chem. Rev.*, 1995, **143**, 611.
5 K. Konishi, *Struct. Bonding*, 2014, **161**, 49.
6 D. M. P. Mingos, *Dalton Trans.*, 2015, **44**, 6680.
7 M. R. Narouz, K. M. Osten, P. J. Unsworth, R. W. Y. Man, K. Salorinne, S. Takano, R. Tomihara, S. Kaappa, S. Malola, C.-T. Dinh, J. D. Padmos, K. Ayoo, P. J. Garrett, M. Nambo, J. H. Horton, E. H. Sargent, H. Häkkinen, T. Tsukuda and C. M. Crudden, *Nat. Chem.*, 2019, **11**, 419.
8 S. Takano and T. Tsukuda, *J. Am. Chem. Soc.*, 2021, **143**, 1683.
9 Y. Niihori, S. Miyajima, A. Ikeda, T. Kosaka and Y. Negishi, *Small Sci.*, 2023, **3**, 2300024.
10 S.-S. Zhang, L. Feng, R. D. Senanayake, C. M. Aikens, X.-P. Wang, Q.-Q. Zhao, C.-H. Tung and D. Sun, *Chem. Sci.*, 2018, **9**, 1251.
11 Y. Shichibu and K. Konishi, *Small*, 2010, **6**, 1216.
12 Y. Shichibu, K. Suzuki and K. Konishi, *Nanoscale*, 2012, **4**, 4125.
13 M. Sugiuchi, Y. Shichibu, T. Nakanishi, Y. Hasegawa and K. Konishi, *Chem. Commun.*, 2015, **51**, 13519.
14 H. Shen, S. Xiang, Z. Xu, C. Liu, X. Li, C. Sun, S. Lin, B. K. Teo and N. Zheng, *Nano Res.*, 2020, **13**, 1908.
15 Z.-H. Gao, J. Dong, Q.-F. Zhang and L.-S. Wang, *Nanoscale Adv.*, 2020, **2**, 4902.
16 H. Hirai, S. Takano, T. Nakashima, T. Iwasa, T. Taketsugu and T. Tsukuda, *Angew. Chem., Int. Ed.*, 2022, **61**, e202207290.
17 E. L. Albright, T. I. Levchenko, V. K. Kulkarni, A. I. Sullivan, J. F. DeJesus, S. Malola, S. Takano, M. Nambo, K. Stamplecoskie, H. Häkkinen, T. Tsukuda and C. M. Crudden, *J. Am. Chem. Soc.*, 2024, **146**, 5759.
18 S. Ito, K. Koyasu, S. Takano and T. Tsukuda, *J. Phys. Chem. Lett.*, 2021, **12**, 10417.
19 H. Shen, Q. Wu, S. Malola, Y.-Z. Han, Z. Xu, R. Qin, X. Tang, Y.-B. Chen, B. K. Teo, H. Häkkinen and N. Zheng, *J. Am. Chem. Soc.*, 2022, **144**, 10844.

20 S.-F. Yuan, Z. Lei, Z.-J. Guan and Q.-M. Wang, *Angew. Chem., Int. Ed.*, 2021, **60**, 5225.
21 K. Isozaki, R. Ueno, K. Ishibashi, G. Nakano, H. Yin, K. Iseri, M. Sakamoto, H. Takaya, T. Teranishi and M. Nakamura, *ACS Catal.*, 2021, **11**, 13180.
22 S. Wang, L. Tang, B. Cai, Z. Yin, Y. Li, L. Xiong, X. Kang, J. Xuan, Y. Pei and M. Zhu, *J. Am. Chem. Soc.*, 2022, **144**, 3787.
23 J. Dong, J. R. Robinson, Z.-H. Gao and L.-S. Wang, *J. Am. Chem. Soc.*, 2022, **144**, 12501.
24 K. Isozaki, K. Iseri, R. Saito, K. Ueda and M. Nakamura, *Angew. Chem., Int. Ed.*, 2023, **63**, e202312135.
25 C. Zhu, Z.-L. Chen, H. Li, L. Lu, X. Kang, J. Xuan and M. Zhu, *J. Am. Chem. Soc.*, 2024, **136**, 23212.
26 K. Ueda, R. Saito, K. Iseri, S. Sekiya, M. Nakamura and K. Isozaki, *ACS Catal.*, 2025, **15**, 12260.
27 L.-J. Liu, X. Lei, J. Guo, X. Mo, Y. Lao, S. Zhuang, H. Zeng, S. Yang, Y. Zhao, W. W. Xu and J. He, *J. Am. Chem. Soc.*, 2025, **147**, 27981.
28 J. Echeverría, D. Casanova, M. Llunell, P. Alemany and S. Alvarez, *Chem. Commun.*, 2008, 2717.
29 P. Liu, R. Qin, G. Fu and N. Zheng, *J. Am. Chem. Soc.*, 2017, **139**, 2122.
30 Y. Du, H. Sheng, D. Astruc and M. Zhu, *Chem. Rev.*, 2020, **120**, 526.
31 R. Jin, G. Li, S. Sharma, Y. Li and X. Du, *Chem. Rev.*, 2021, **121**, 567.
32 S. Masuda, K. Sakamoto and T. Tsukuda, *Nanoscale*, 2024, **16**, 4514.
33 T. Müller, K. Hultzsch, M. Yus, F. Foubelo and M. Tada, *Chem. Rev.*, 2008, **108**, 3795.
34 Y. Lu, Y. Wang, H. Li, P. Li, X. Feng, Y. Yamamoto, M. Bao and J. Liu, *RSC Adv.*, 2023, **13**, 3371.
35 A. D. Litta, A. Buonerba, A. Casu, A. Falqui, C. Capacchione, A. Franconetti, H. Garcia and A. Grassi, *J. Catal.*, 2021, **400**, 71.
36 V. I. Isaeva, K. Papathanasiou, V. V. Chernyshev, L. Glukhov, G. Deyko, K. K. Bisht, O. P. Tkachenko, S. V. Savilov, N. A. Davshan and L. M. Kustov, *ACS Appl. Mater. Interfaces*, 2021, **13**, 59803.
37 M. Boundor, N. Katir, S. Royer and A. El Kadib, *ACS Appl. Nano Mater.*, 2025, **8**, 639.
38 (*a*) CCDC 2481066: Experimental Crystal Structure Determination, 2025, DOI: **10.5517/ccdc.csd.cc2p8rd4**; (*b*) CCDC 2484473: Experimental Crystal Structure Determination, 2025, DOI: **10.5517/ccdc.csd.cc2pd99q**; (*c*) CCDC 2484474: Experimental Crystal Structure Determination, 2025, DOI: **10.5517/ccdc.csd.cc2pd9br**.